Effects of energetic large-scale coherent structures on wall mass transfer rate of turbulent flow behind orifice in round pipe

Feng Shan
School of Energy and Power Engineering
Huazhong University of Science and Technology
Wuhan, 430074, China
shanfeng@hust.edu.cn

Zhiqiang Yu
School of Energy and Power Engineering
Huazhong University of Science and Technology
Wuhan, 430074, China
onoryu@foxmail.com

Kano Masashi
Department of Energy Engineering and Science
Nagoya University
Nagoya 464-8603, Japan
kanomashshi@ees.nagoya-u.ac.jp

Yoshiyuki Tsuji
Department of Energy Engineering and Science
Nagoya University
Nagoya 464-8603, Japan
c42406@cc.nagoya-u.ac.jp

ABSTRACT

This paper first uses a low-speed stereoscopic particle image velocimetry (SPIV) system to measure the convergent statistical quantities of the flow field and then simultaneously measure the time-resolved flow field and the wall mass transfer rate by a high-speed SPIV system and an electrochemical system, respectively. We measure the flow field and wall mass transfer rate under the upstream pipe Reynolds numbers between 25000 and 55000 at three specific locations behind the orifice plate. Moreover, we apply proper orthogonal decomposition (POD), stochastic estimation, and spectra analysis to study the properties of the flow field and the wall mass transfer rate. More importantly, we investigate the large-scale coherent structures' effects on the wall mass transfer rate. The collapse of the wall mass transfer rates' spectra by the corresponding time scales at the three specific positions of orifice flow suggests that the physics of low-frequency wall mass transfer rates are probably the same, although the flow fields away from the wall are pretty different. Furthermore, the spectra of the velocity reconstructed by the most energetic eigenmodes agree well with the wall mass transfer rate in the low-frequency region, suggesting that the first several energetic eigenmodes capture the flow dynamics relevant to the low-frequency variation of the wall mass transfer. Stochastic estimation results of the velocity field associated with large wall mass transfer rate at all three specific locations further reveal that the most energetic coherent structures are correlated with the wall mass transfer rate.

INTRODUCTION

Orifice plates widely exist in many piping systems in the energy and chemical industry. The turbulent flow field behind a circular orifice plate in a round pipe (hereafter referred to as orifice flow in short) is a typical separated internal flow, where flow separation and reattachment occur with strong three-dimensional complex properties, as shown in figure 1. It is of immense importance in many practical fields; for instance, flow-accelerated corrosion (FAC), also known as flow-assisted corrosion, usually occurs in the near field. FAC is a corrosion mechanism in which an ordinarily protective oxide layer on a metal surface dissolves in fast-flowing water. As a result, the pipe wall thickness decreases because of FAC.

Moreover, the pipe wall thickness in the near field downstream of the orifice plate is not even with the appearance of the thinnest pipe wall location. Consequently, pipe rupture usually occurs in the thinnest pipe wall location, which has caused many serious accidents worldwide. Although the decrease of pipe wall thickness behind an orifice is combined with material, chemistry, and hydrodynamic conditions, the orifice plate's strongly turbulent flow field is believed to accelerate the decrease of the pipe wall thickness, which motivates the present study.

So far, many researchers believe that the position of the maximum wall mass transfer rate is close to the position of the maximum streamwise velocity fluctuation (or the maximum turbulent kinetic energy) in orifice flow, and some further argue that it should be located near the reattachment point. However, we find this is not true, at least in the Reynolds number region 25000~55000. Furthermore, how the large-scale energetic coherent structures evolve in this strongly developing flow is missing in previous studies of this rapidly developing separated internal flow. The effects of the large-scale energetic coherent structures on the wall mass transfer rate are also missing in the literature. Understanding these effects helps reveal the mechanisms of wall mass transfer augmentation and the appearance of the large wall mass transfer rate position in the near field of orifice flow, which is beneficial for preventing FAC problems. The coherent structures are also expected to play essential roles in macro-characteristics of the flow and processes such as scalar and momentum transport, chemical mixing, and noise generation. Trying to understand these structures' spatial and temporal evolution has become paramount to understanding the process by which heat, mass, and momentum are transferred through the mean flow (Tinney et al., 2008).

In the current study, we rely on the mixed Fourier and POD techniques to extract the large-scale energetic coherent structures in orifice flow. We adopt this method is mainly because of its successful use in a pipe flow and a sudden pipe expansion (Tinney et al., 2006), which is another typical separated internal flow and shares many similar characteristics of the flow field. In general, our research aim is twofold. The first aim is to extract the large-scale coherent structures at three typical locations in the near field of orifice flow to understand the evolution of the coherent structures in orifice flow, and the second aim is to find out the possible role of these large-scale coherent structures on the wall mass transfer rate.

EXPERIMENTAL SETUP

In the present study, we carried out two sets of experiments, one was the measurements of independent instantaneous velocity fields by a low-speed SPIV system, and another was the simultaneous measurements of the time-resolved velocity field and the wall mass transfer rate by the combination of a high-speed SPIV system and an electrochemical system. Using the low-speed SPIV system, we measured the independent velocity fields for a sufficiently long time to get convergent orifice flow statistics. We simultaneously measured the velocity field and wall mass transfer rate at a relatively high speed for a short period. In this case, we can analyze the flow field's dynamical properties and the relationships between the flow field and the wall mass transfer rate.

Figure 2 shows the sketch of the flow recirculation loop for measurements of the velocity field and the wall mass transfer rate. A gas container filled with high-pressure nitrogen is connected to the water tank to remove the oxygen in the flow recirculation loop before the simultaneous velocity field and wall mass transfer rate measurements. A centrifugal pump drove the working fluid in the tank to recirculate inside a piping system of inner diameter 46 ± 0.1mm. There is a square-edged orifice plate with a thickness of 5 mm located inside the piping system. The orifice to pipe diameter ratio $\beta \equiv d/D = 0.62$, where d and D are the orifice and pipe diameters, respectively. We measured the flow fields at two upstream pipe Reynolds numbers $Re_D = U_b D / \nu = 25000$ and 55000, where U_b is the bulk velocity and ν is the kinematic viscosity. The straight pipe's length upstream of the orifice plate was approximately $74D$; and the length of the straight pipe downstream of the orifice was approximately $15D$, as can be seen in figure 2. The flow achieves a fully developed pipe flow far upstream of the orifice plate.

We specially designed a test section in figure 3 to measure the velocity field and the wall mass transfer rate simultaneously. A handcrafted trigger box (not shown here) triggered the simultaneous measurements of the velocity field and the wall mass transfer rate. An acrylic water jacket and two prisms filled with water were adopted to minimize the optical distortion due to refraction through the pipe wall. The test section housed several electrodes, separated into three groups: the working electrodes, the counter electrode, and the reference electrode. All electrodes were mounted flush with the pipe wall; therefore, no abrupt change of the hydrodynamic conditions occurred in the connection region between the electrodes and the pipe wall.

The working electrodes were constructed by inserting a cylindrical gold wire with a diameter of 1 mm into the pipe wall. There are 20 working electrodes evenly distributed from $x/D = 0.1 \sim 2$; thus, the distance between two neighboring electrodes is $0.1D$, as shown in Figure 3. The counter electrode was a nickel circular ring with a length of 5 mm. The much larger size of the counter electrode than the working electrodes was selected to ensure that the current flowing into the circuit was controlled by the working electrode's surface reactions. The counter and reference electrodes were located approximately five and eight times the pipe diameter away from the orifice's downstream surface, respectively. The original coordinate system of the raw PIV data is Cartesian coordinate with the origin in the center of the orifice plate's downstream surface, as shown in figure 3. Vz, Vy, and Vx represent the instantaneous spanwise, vertical, and streamwise velocities, respectively. However, to use the mean velocity field's axisymmetric property in the azimuthal direction, the original velocity field is interpolated into a cylindrical coordinate system using Vr, Va, and Vx to represent the instantaneous radial, azimuthal, and streamwise velocity components, respectively.

In the present study, one working electrode was selected with the counter electrode to form a current circuit to measure the local wall mass transfer rate. The working electrodes act as the cathode. The counter electrode acts as the anode and requires a known potential to balance the charge added or removed by the working electrode. The reference electrode was used as an anode with a known reduction potential. Its only use was to act as a reference when measuring and controlling the working electrode's potential; it did not pass any current.

A carefully configured chemical solution with the fluorescent particles was used as working fluid in the flow recirculation loop, as shown in Figure 2. The fluorescent particles Fluostar with a mean diameter of 15 μm and density of 1.1 g/cm^3 is commercially available from Kanomax Company. The use of fluorescent particles was aimed at reducing the strong laser reflection from the pipe wall. To record only the fluorescent light reflected by the fluorescent particles, two long-pass filters ($\lambda_L > 580$ nm) were mounted in front of the two lenses in the SPIV measurement.

The test solution was an equilibrium mixture of potassium ferricyanide ($K_3Fe(CN)_6$) and potassium ferrocyanide ($K_4Fe(CN)_6$) with potassium sulfate (K_2SO_4) as the supporting electrolyte, whose ions were not involved in the electrode reactions. De-ionized water and high purity chemicals (analytical reagent) were used to make up $90\,L$ solutions. The temperature of the electrolyte was maintained at $20\,℃$ throughout the measurements. Precautions were taken to avoid contamination of both electrolyte and electrode surfaces. More specifically, the solution was protected as much as possible from exposure to daylight, and the solution was de-aerated and kept under a blanket of inert nitrogen gas. For more details of the mass transfer measurement, please refer to Tong et al. (2018).

DATA ANALYSIS METHOD

The mixed Fourier and POD process in the present study is very similar to those used in many previous studies, see, for instance, Hellstrom and Smits (2014). The determination of the large wall mass transfer rate is subjective. Since we are discussing the fluctuations of wall mass transfer below, we define the condition of the large wall mass transfer rate the fluctuation of wall mass transfer rate larger than five times its root mean square. Stochastic estimation can estimate the conditionally averaged velocity field with much less data. Adrian (1977)first proposed its application to extract coherent motion in turbulent flows. Since then, it has been widely used in the community of fluid dynamics, where the velocity field or pressure has been primarily used as the condition to perform the stochastic estimation.

RESULTS AND DISCUSSIONS

Based on the experimental data(Shan et al., 2013), we replot the mean streamline pattern in the radial-streamwise plane and the mean wall mass transfer rate profile as shown in Figure 4. One can observe the secondary and primary recirculation regions from the mean streamline patterns shown in the sketch of orifice flow in Figure 1. The four red lines represent the location at which the mean streamwise velocity $\overline{V}_x = 0$. These lines can be considered the mean reattachment lines separating the positive and negative mean streamwise velocities. Quantitatively, the two mean reattachment lengths of this flow are located approximately at $x_{r1} = 3.64R$ and $x_{r2} = 0.26R$, respectively. The three bold green lines illustrate the positions of the three cross-sections in the present study. We selected the three cross-sections $x_1 = 0.2R$, $x_2 = 2R$ and $x_3 = 4R$, locating at three

typical positions of this separated internal flow. More specifically, the three locations are located in the secondary recirculation, the primary recirculation and the redevelopment regions, respectively.
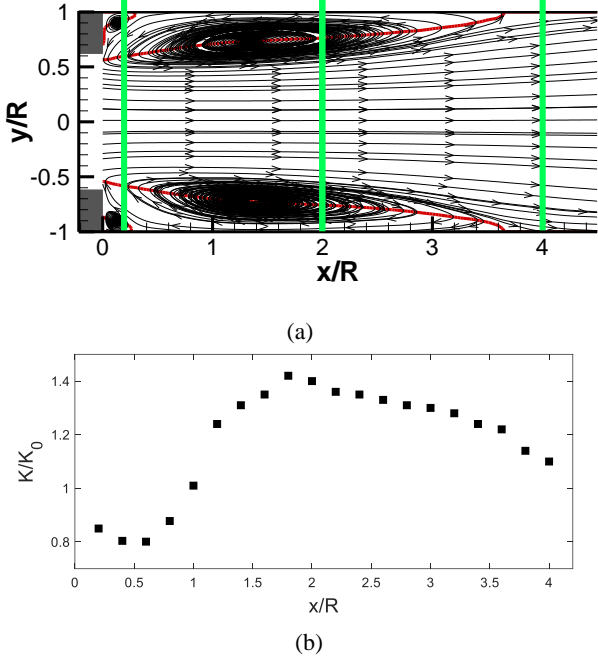

(a)

(b)

Figure 4. (a) mean streamline pattern and (b) profile of mean wall mass transfer downstream of orifice flow normalized by the value of fully developed pipe flow: the three green lines illustrate the laser sheet positions; K and K_0 represent the mean wall mass transfer rate in the orifice flow and the fully developed pipe flow, respectively.

The profile of the mean wall mass transfer rate downstream of the orifice plate shown in Figure 4 (b) shows that the wall mass transfer rate is far from uniform in the near field downstream of the orifice, which would result in a non-uniform pipe wall thickness. Moreover, the wall mass transfer rate in the primary recirculation region downstream of one pipe radius ($\sim 1 < x/R < \sim 3.5$) is enhanced compared with that of fully developed pipe flow ($K/K_0 > 1$), and the maximum mean wall mass transfer rate position is located near $x/R = 2$. The maximum mean wall mass transfer rate position agrees very well with the thinnest pipe wall location in the industry.

We measured the wall mass transfer rate corresponding to the above three positions in the simultaneous measurements of the velocity field and the wall mass transfer rate. Figure 5 shows the spectra of the wall mass transfer rate fluctuations normalized by the typical time scale Δt_0, which is defined based on the auto-correlation function of the wall mass transfer rate,

$$c(\Delta t) = \frac{\langle k(t)k(t+\Delta t) \rangle}{\sigma^2}. \quad (1)$$

The typical time scale Δt_0 is given by the zero-crossing of the autocorrelation curve

$$\Delta t_0 = \Delta t|_{c(\Delta t)=0}. \quad (2)$$

One can observe that the spectra at three different positions match very well in the low-frequency region ($f\Delta t < 10$) when normalized by the corresponding time scales. The wall mass transfer rate may be contaminated by high-frequency electrical noise; therefore, the wall mass transfer rate fluctuation was filtered by a low-pass filter (Tong et al., 2018). However, we are only interested in the low-frequency wall mass transfer fluctuation; thus, no filter was used in the present study. The

collapse of the wall mass transfer spectra in the low-frequency region suggests that it probably follows the same physics in the wall region though the flow fields at these three locations far from the wall are pretty different.
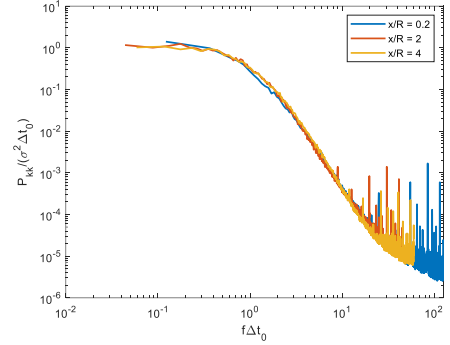

Figure 5. Normalized spectra of wall mass rate at the three typical positions.

To analyze the relationship between the velocity field and the wall mass transfer rate statistically, we calculate the velocity and wall mass transfer rate spectra. The spectra for both the original velocity and the velocity reconstructed by the most energetic POD eigenmodes are compared with the wall mass transfer rate spectrum. The velocity spectra for all three components are normalized by the corresponding variances and the typical time scales of the wall mass transfer rate, and the velocity spectra are averaged in the azimuthal direction.

Figure 6 shows the power spectra density of the wall mass transfer rate and the azimuthal velocities for different radial positions at the cross-section $x/R = 0.2$. The original velocity spectra shown in figure 6 (a) can be divided into three groups, i.e., the spectra in the core, shear layer, and recirculation regions, respectively. The black and green solid lines representing the velocity spectra in the recirculation region have similar profiles. The cyan line represents the velocity in the shear layer region and has a small peak around non-dimensional frequency 20, probably the typical frequency of the vortex shedding in the shear layer region. Note that this peak is more evident in the spectra of the radial and the streamwise velocities 6. The velocity spectra in the core and shear layer regions (the red and blue solid lines) are very different from the wall mass transfer rate spectrum (the black dashed line) since they are relatively far away from the wall mass transfer rate measurement sensor. However, velocity spectra in the recirculation region (the solid green and black lines) are similar to the wall mass transfer rate spectrum in the low-frequency region, suggesting that the low frequency (large time scale) flow structures probably have a relationship with the wall mass transfer rate. However, the profile of the wall mass transfer spectra starts to differ from that of the velocity in the non-dimensional frequency region $f\Delta t_0 > 2$.

Figure 6 (b) shows the spectra of the wall mass transfer rate and the velocity reconstructed by the ten most energetic POD eigenmodes, accounting for approximately 33 % of the turbulent kinetic energy. The reconstructed velocity spectra can still be divided into three groups similar to the original velocity spectra. However, noticeable differences between the original and reconstructed velocity spectra also appear. For instance, the reconstructed velocity spectra in the core and shear layer regions have small peaks around non-dimensional frequency 20. We assume that this frequency is related to the large-scale coherent structures in the secondary recirculation region. Although the

3

original velocity spectra in the shear and core regions (the red, blue, and cyan lines) do not agree with the wall mass transfer rate spectrum, all the spectra of the velocity reconstructed by the most energetic POD eigenmodes agree reasonably well with the wall mass transfer rate spectrum in the low-frequency region ($f\Delta t_0 < 2$), especially the reconstructed velocity spectra in the recirculation region (the black and green solid lines). This result reveals that the low-frequency wall mass transfer rate fluctuation is probably related to the large-scale energetic coherent structures.
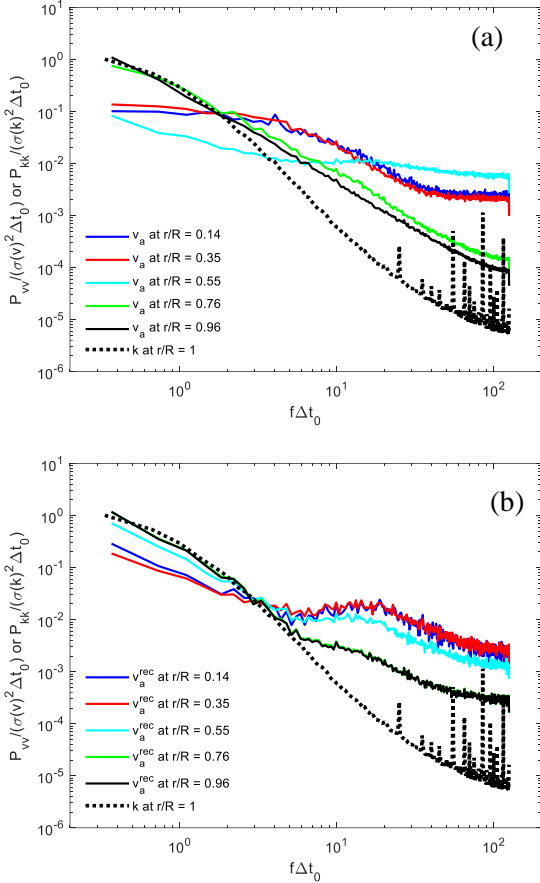
Figure 6. Spectra of the wall mass transfer rate and azimuthal velocity for different radial positions (r/R = 1 is the pipe wall) at the streamwise position x/R = 0.2: (a) wall mass transfer and original velocity; (b) wall mass transfer rate and reconstructed velocity using ten most important eigenmodes. The superscript "rec" represents the reconstructed velocity.

Figures 7 and 8 show the spectra of the wall mass transfer and the azimuthal velocity at the cross-sections $x/R = 2$ and $x/R = 4$, respectively. The selection of different numbers of POD eigenmodes to reconstruct the velocity field is based on the energy profile of the POD eigenmodes. The solid black line representing the original velocity spectrum in the near-wall region at the cross section $x/R = 2$ has similar profiles as that of the wall mass transfer rate in the low-frequency region ($f\Delta t_0 < 2$) as shown in figure 7(a), which suggests that the dynamical properties of velocity field in the low-frequency region at the cross section $x/R = 2$ are similar to that of the wall mass transfer rate. Additionally, the low-frequency region of the velocity spectra can be reconstructed by the large-scale energetic eigenmodes (80 modes in the present case), as shown in figure 7 (b). The blue and red lines representing the original velocity spectra in the shear layer regions peak around $f\Delta t_0 \approx 3$ in figure

17, which we assume is probably related to the vortex shedding property in the shear layer region.

One can also observe from figure 8 (a) that the solid black line representing the original velocity spectrum in the near-wall region at the cross section $x/R = 4$ agrees with the wall mass transfer spectrum in the low-frequency region ($f\Delta t_0 < 2$). Moreover, this spectrum can be reconstructed by the large-scale energetic POD eigenmodes if one compares figures 8 (a) and (b). Note that the red and blue lines in figure 8 (a) representing the original azimuthal velocity spectra show a small peak around $f\Delta t_0 \approx 2$. However, the original streamwise velocity spectra do not have this peak. We assume that this peak is probably related to the shear layer reattachment process.
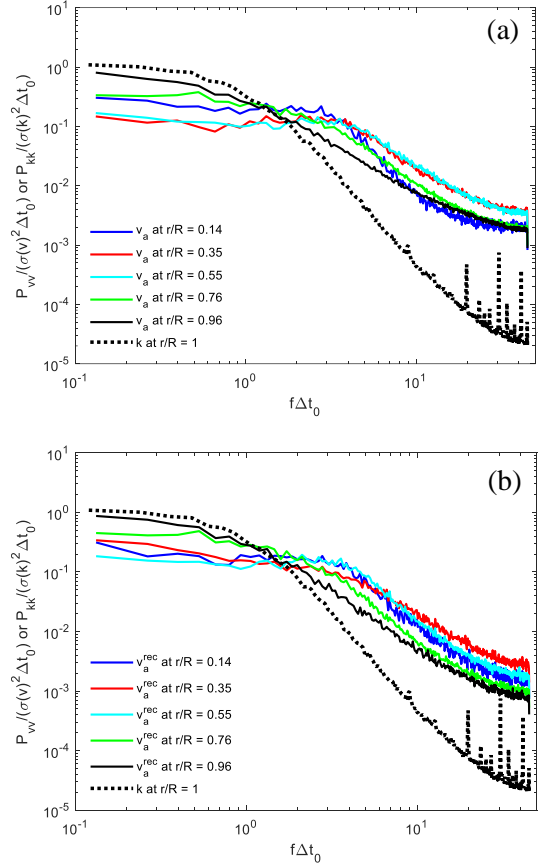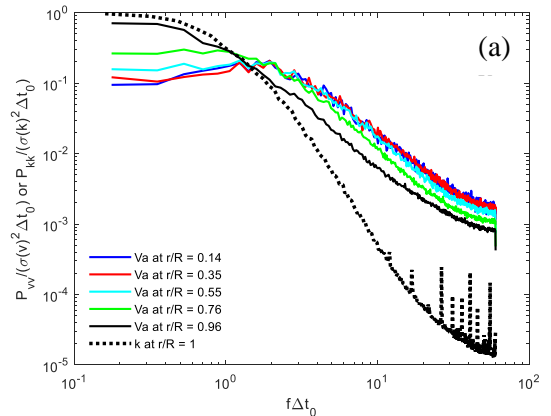

Figure 7. Spectra of the wall mass transfer rate and the azimuthal velocity at different radial positions (r/R = 1 is the pipe wall) at streamwise position x/R = 2: (a) wall mass transfer and original velocity; (b) wall mass transfer rate and reconstructed velocity using 80 most important eigenmodes.
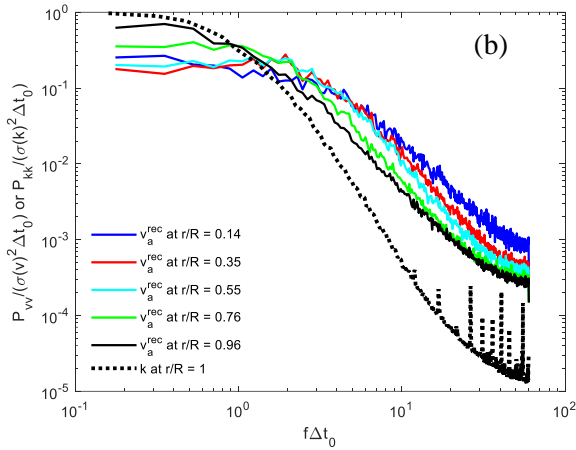
Figure 8. spectra of wall mass transfer rate and azimuthal velocity at different radial positions (r/R = 1 is the pipe wall) at streamwise position x/R = 4: (a) wall mass transfer and original velocity; (b) wall mass transfer rate and reconstructed velocity using 50 most important eigenmodes.

We find out from the above discussions that the wall mass transfer rate spectra agree reasonably well with the spectra of velocity reconstructed by the most energetic eigenmodes in the low-frequency region at all three specific cross-sections. We thus assume that the large-scale energetic coherent structures' frequency properties are related to those of the wall mass rate. In other words, the energetic coherent structures are probably related to the low-frequency variation of the wall mass transfer rate in the near field of orifice flow.

Figure 9 shows the quadratic stochastic estimation of the conditionally averaged flow field associated with the large wall mass transfer rate ($k > 5\,k_{rms}$) at all three cross-sections, where k is the wall mass transfer rate fluctuation and k_{rms} is the root mean square of the fluctuation. One can observe from figure 19 (a) that large-scale azimuthal velocity patterns with opposite directions appear in the conditional averaged flow field. In addition, the background contour shows the high-speed fluid flanked by low-speed fluid. If we compare figure 9 (a) with the samples of the several most energetic POD eigenmodes shown in figure 10, we can observe that the first three most energetic POD eigenmodes show similar velocity patterns. The difference is that the scale of the velocity patterns in the azimuthal direction may be different. Figures 9 (b) and (c) show similar counter-rotating vortex pairs in the conditional averaged velocity fields associated with large wall mass transfer rates. All the most energetic POD eigenmodes at the cross-sections $x/R = 2$ and $x/R = 4$ show counter-rotating vortex pairs of different radial and azimuthal scales. In addition, the distribution of the streamwise velocity shown as the background contour is also similar. More specifically, there are high-speed regions flanked by low-speed regions for both two cross-sections. We believe that comparing the stochastic estimation results in figure 19 and the most energetic POD eigenmodes reveals evidence of the strong effects of the large-scale energetic coherent structures on the wall mass transfer rate at all three specific cross-sections in the near field orifice flow. Note that the counter-rotating vortex pairs enhancing the wall mass transfer rate here in figures 19 (b) and (c) are very similar to the flow structures enhancing the wall shear stress (Tong et al., 2020) in a pipe flow and the sketch of large-scale coherent flow motions in the boundary layer of wall-bounded flow (Marusic et al., 2010).
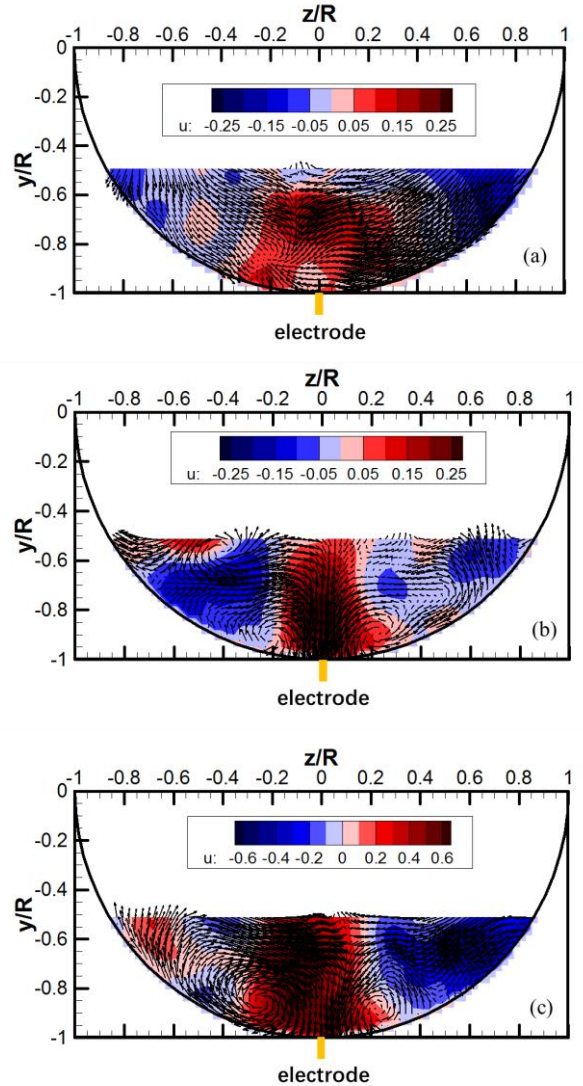

Figure 9. Stochastic estimation of the conditional averaged flow structures associated with large wall mass transfer rate at: (a) cross section x/R =0.2; (b) cross section x/R=2; (c) cross section x/R = 4.

REFERENCES

Adrian, R. J. (1977). *On the role of conditional averages in turbulence theory*.

Hellstrom, L., & Smits, A. (2014). The energetic motions in turbulent pipe flow. *Physics Of Fluids [P]*, *26*(12), 1-10.

Marusic, I., Mathis, R., & Hutchins, N. (2010). Predictive model for wall-bounded turbulent flow. *Science*, *329*(5988), 193-196.

Shan, F., Fujishiro, A., Tsuneyoshi, T., & Tsuji, Y. (2013). Particle image velocimetry measurements of flow field behind a circular square-edged orifice in a round pipe. *Experiments in fluids*, *54*(6), 1553.

Tinney, C., Glauser, M., Eaton, E., & Taylor, J. (2006). Low-dimensional azimuthal characteristics of suddenly expanding axisymmetric flows. *Journal of Fluid Mechanics*, *567*, 141-155.

Tinney, C. E., Glauser, M. N., & Ukeiley, L. S. (2008). Low-dimensional characteristics of a transonic jet. Part 1. Proper orthogonal decomposition. *Journal of Fluid Mechanics*, *612*, 107-141. https://doi.org/10.1017/S0022112008002978

Tong, T., Bhatt, K., Tsuneyoshi, T., & Tsuji, Y. (2020). Effect of large-scale structures on wall shear stress fluctuations in pipe flow. *Physical Review Fluids*, *5*(10), 104601.

Tong, T., Tsuneyoshi, T., Ito, T., & Tsuji, Y. (2018). Instantaneous mass transfer measurement and its relation to large-scale structures in pipe flow. *International Journal of Heat and Fluid Flow*, *71*, 160-169.
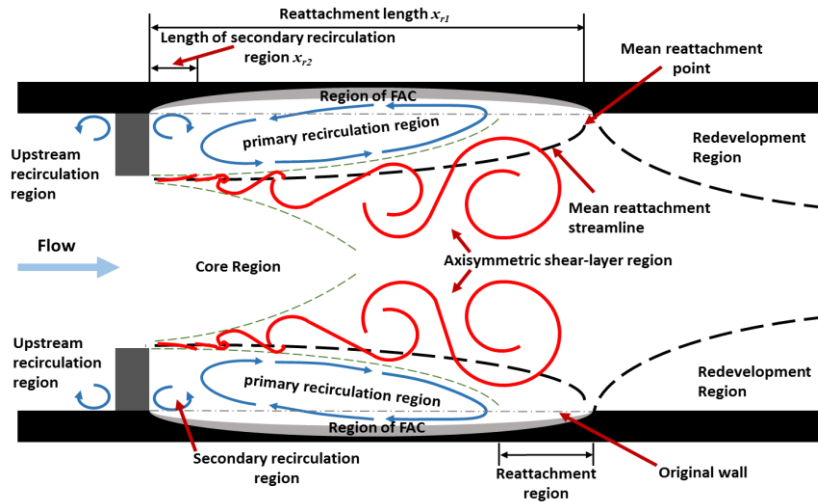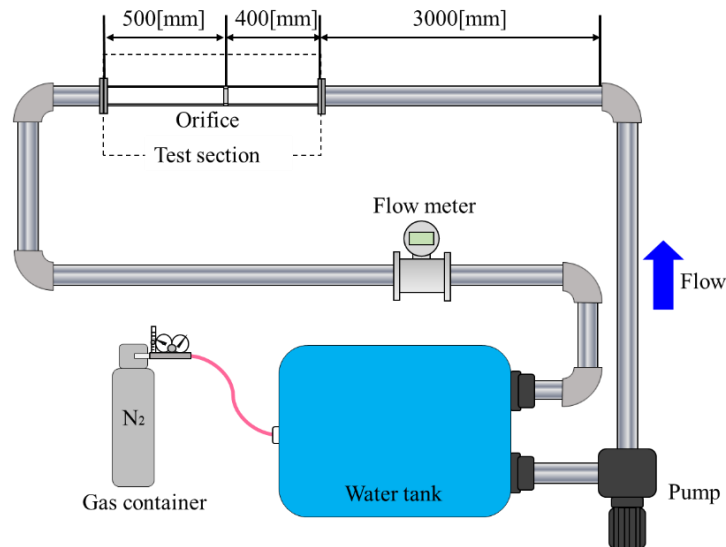
Figure 1. Sketch of orifice flow and FAC problem.

Figure 2. Sketch of the flow recirculation loop for measurements of the flow field and the wall mass transfer rate.
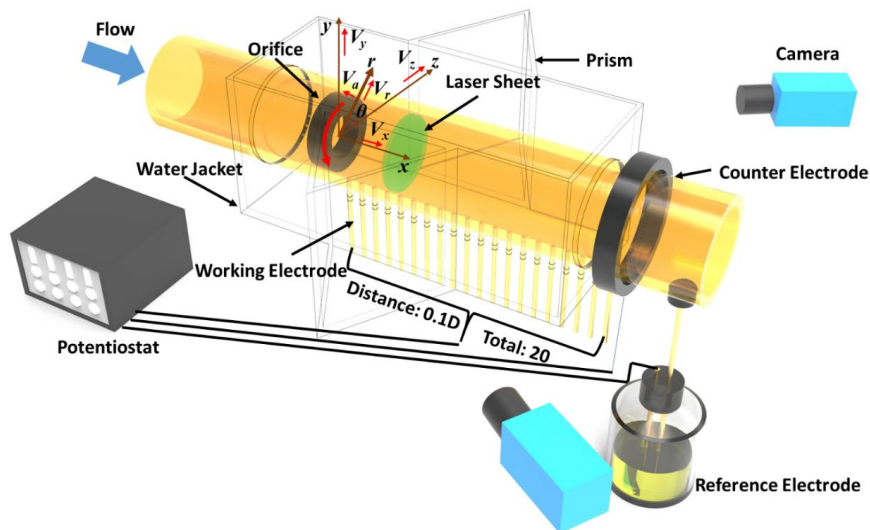

Figure 3.Test section for simultaneous measurements of the velocity field and the wall mass transfer rate.